4-2013

Testing galaxy formation models with the GHOSTS survey : the color profile of M81's stellar halo.

Antonela Monachesi
University of Michigan-Ann Arbor

Eric F. Bell
University of Michigan-Ann Arbor

David J. Radburn-Smith
University of Washington - Seattle Campus

Marija Vlajic
Leibniz-Institut fur Astrophysik Potsdam

Roelof S. de Jong
Leibniz-Institut fur Astrophysik Potsdam

See next page for additional authors

Original Publication Information

Authors

Antonela Monachesi, Eric F. Bell, David J. Radburn-Smith, Marija Vlajic, Roelof S. de Jong, Jeremy Bailin, Julianne J. Dalcanton, Benne W. Holwerda, and David Streich

TESTING GALAXY FORMATION MODELS WITH THE GHOSTS SURVEY: THE COLOR PROFILE OF M81's STELLAR HALO[*]

Antonela Monachesi[1], Eric F. Bell[1], David J. Radburn-Smith[2], Marija Vlajić[3], Roelof S. de Jong[3],
Jeremy Bailin[1], Julianne J. Dalcanton[2], Benne W. Holwerda[4,5], and David Streich[3]
[1] Department of Astronomy, University of Michigan, 830 Dennison Building, 500 Church Street, Ann Arbor, MI 48109, USA; antonela@umich.edu
[2] Department of Astronomy, University of Washington, Seattle, WA 98195, USA
[3] Leibniz-Institut für Astrophysik Potsdam, D-14482 Potsdam, Germany
[4] European Space Agency, ESTEC, Keplerlaan 1, 2200 AG Noordwijk, The Netherlands
Received 2012 September 18; accepted 2013 February 8; published 2013 March 14

ABSTRACT

We study the properties of the stellar populations in M81's outermost part, which hereafter we will call the stellar halo, using *Hubble Space Telescope* (*HST*) Advanced Camera for Surveys observations of 19 fields from the GHOSTS survey. The observed fields probe the stellar halo out to a projected distance of ∼50 kpc from the galactic center. Each field was observed in both $F606W$ and $F814W$ filters. The 50% completeness levels of the color–magnitude diagrams (CMDs) are typically at 2 mag below the tip of the red giant branch (TRGB). Fields at distances closer than 15 kpc show evidence of disk-dominated populations whereas fields at larger distances are mostly populated by halo stars. The red giant branch (RGB) of the M81's halo CMDs is well matched with isochrones of ∼10 Gyr and metallicities [Fe/H] ∼ −1.2 dex, suggesting that the dominant stellar population of M81's halo has a similar age and metallicity. The halo of M81 is characterized by a color distribution of width ∼0.4 mag and an approximately constant median value of ($F606W − F814W$) ∼ 1 mag measured using stars within the magnitude range $23.7 \lesssim F814W \lesssim 25.5$. When considering only fields located at galactocentric radius $R > 15$ kpc, we detect no color gradient in the stellar halo of M81. We place a limit of 0.03 ± 0.11 mag difference between the median color of RGB M81 halo stars at ∼15 and at 50 kpc, corresponding to a metallicity difference of 0.08 ± 0.35 dex over that radial range for an assumed constant age of 10 Gyr. We compare these results with model predictions for the colors of stellar halos formed purely via accretion of satellite galaxies. When we analyze the cosmologically motivated models in the same way as the *HST* data, we find that they predict no color gradient for the stellar halos, in good agreement with the observations.

Key words: galaxies: halos – galaxies: individual (M81) – galaxies: spiral – galaxies: stellar content

Online-only material: color figures

1. INTRODUCTION

According to the currently favored cosmological model, ΛCDM, galaxies form hierarchically through the accretion of smaller objects that, due to gravity, merge together to form the larger systems we see today (e.g., White & Rees 1978). Predictions of this theory, such as the existence of coherent streams, shells, satellite galaxies, and other substructure in the halos of galaxies (Johnston et al. 1996; Helmi & White 1999; Helmi & de Zeeuw 2000; Bullock et al. 2001; Bullock & Johnston 2005; De Lucia & Helmi 2008; Gómez et al. 2010; Cooper et al. 2010) have been supported by observations not only in our own Galaxy (Ibata et al. 1995, 2003; Helmi et al. 1999; Majewski et al. 2003; Yanny et al. 2003; Belokurov et al. 2006; Jurić et al. 2008; Bell et al. 2008; Grillmair 2009), but also in M31 (Ibata et al. 2007; McConnachie et al. 2009), and in more distant galaxies (e.g., Martínez-Delgado et al. 2009, 2010; Mouhcine et al. 2010; Bailin et al. 2011).

Another important prediction provided by theoretical models is the existence of stellar population variations within stellar halos (Robertson et al. 2005; Font et al. 2006a, 2008; Cooper et al. 2010; Tumlinson 2010). Metallicity variations are expected

due to the mass–metallicity relation assumed for the accreted satellite galaxies in the models, such that more massive satellites have higher metallicities. Age variations are also expected due to the differences in the satellite accretion times.

The halo of our own Galaxy has been extensively studied and variations of its stellar populations have been detected (e.g., Ivezić et al. 2008). Bell et al. (2010) have used the ratio of blue horizontal-branch stars to main-sequence turnoff stars from the Sloan Digital Sky Survey (SDSS; York et al. 2000) to show that large stellar population variations can be detected out to heliocentric distances of ∼30 kpc. Moreover, they found that these variations trace different previously identified structures. In M31, variations in the halo's stellar populations have also been detected using deep *Hubble Space Telescope* (*HST*) observations (Brown et al. 2006; Richardson et al. 2008, 2009; Sarajedini et al. 2012). These variations were associated with substructures detected from ground-based observations (Ibata et al. 2007; McConnachie et al. 2009).

Even though stellar population variations are present throughout the stellar halos of both the Milky Way and M31, the existence of metallicity gradients is still a matter of debate. For the Milky Way, recent studies have analyzed different stellar samples from the SDSS; Carollo et al. (2007, 2010) detected variations on the mean metallicity with distance from the Galactic plane, with stars at $R < 15$ kpc more metal-rich ([Fe/H] ∼ −1.6) than those at larger radii ($R > 15$–20 kpc) with an average metallicity of [Fe/H] ∼ −2.2 dex. They

considered a sample of halo stars located in the solar neighborhood, but reaching the outer regions of the halo in their orbits. They suggested the existence of two distinct components of the halo, i.e., inner and outer halo. Ivezić et al. (2008) used a large sample of stars that reach to 8 kpc from the Sun and found a mean metallicity of [Fe/H] ~ -1.46 dex with a nearly flat radial metallicity gradient. They assume that their sample, however, is likely to be dominated by inner halo stars. Using photometric data from the SDSS/SEGUE survey, de Jong et al. (2010) constructed a color–magnitude diagram (CMD) of Milky Way thick disk and halo stars that are at $|Z| > 1$ kpc from the Galactic plane. They adopted a single age of ~ 14 Gyr and three metallicity bins of [Fe/H] $= -0.7, -1.3,$ and -2.2 to fit the turnoff stars of their CMD, presuming that those three components are sufficient to fully describe both the thick disk and halo stars of their sample. They found a mean halo metallicity of [Fe/H] $= -1.6$ at distances smaller than 10 kpc and a mean metallicity of [Fe/H] $= -2.2$ for the stellar halo at distances larger than 15 kpc, consistent with the results of Carollo et al. (2007). A more recent study, however, utilizes an "in situ" sample of K giants from SDSS/SEGUE spectroscopic observations and show a nearly flat Galactic halo metallicity distribution ([Fe/H] ~ -1.4 dex) within ~ 20 to ~ 60 kpc (Ma et al. 2012; Z. Ma et al., in preparation). We recognize, nevertheless, that all the mentioned studies may have important biases introduced by, e.g., the magnitude or color limit considered, which affect the determination of a metallicity–distance relation and need to be carefully taken into account (see, e.g., Schönrich et al. 2011; Beers et al. 2012). More studies are needed to understand the properties of the Milky Way halo. Future surveys, such as *Gaia* (Perryman et al. 2001), LAMOST (Large Sky Area Multi-Object Fiber Spectroscopic Telescope; Newberg et al. 2009), and LSST (Large Synoptic Survey Telescope; Tyson 2002) will help to shed light on this matter.

For M31, halo metallicity studies have probed regions at much farther radii than for the Milky Way. Kalirai et al. (2006) and Koch et al. (2008) have detected a clear metallicity gradient over a large range of radial distances, from ~ 10 kpc to ~ 160 kpc, with significant scatter around this overall trend. Kalirai et al. (2006) found a mean metallicity of [Fe/H] $\sim -0.5,$ $\sim -0.95,$ and ~ -1.26 dex, at average projected distances of 14 kpc, 31 kpc, and 81 kpc from M31's center, respectively, from photometric properties of spectroscopically selected M31 red giant branch (RGB) bulge+halo stars. Koch et al. (2008) studied a spectroscopic sample of M31's halo stars along the minor axis from 9 to 160 kpc and found a strong metallicity gradient, with a sharp decline of ~ 0.5 dex at ~ 20 kpc, using the spectral CaT lines. However, several studies have found no evidence of such gradient (e.g., Durrell et al. 2004; Irwin et al. 2005; Chapman et al. 2006; Richardson et al. 2009). Among the latest works, Chapman et al. (2006) selected a spectroscopic sample of M31's halo stars by kinematically isolating nonrotating stars, and found a metal-poor metallicity of [Fe/H] ~ -1.4 dex with no detectable metallicity gradient from 10 to 70 kpc. Using 11 very deep *HST* fields of M31's halo, Richardson et al. (2009) found that there is no evidence of a radial metallicity gradient within ~ 30–60 kpc. They calculated an average metallicity over that range of [Fe/H] $= -0.8 \pm 0.14$ using the photometric properties of RGB stars. The differences among the data analyzed and methods used to analyze it, as well as the different various halo regions probed, make it difficult to completely disentangle why the results, mainly in the inner 60 kpc, are so diverse. In general, nevertheless, the inner ~ 15–50 kpc region of M31's halo shows a nearly flat, high-metallicity profile ([Fe/H] ~ -0.8 dex), whereas outside ~ 60 kpc the metallicities are lower ([Fe/H] ~ -1.3 dex).

While the Milky Way and M31 agree qualitatively with the model predictions of stellar halo formation, they exhibit clear differences. For instance, the M31 outer halo is more metal-rich by a factor of three or more than that of the Milky Way out to at least 60 kpc (Richardson et al. 2009). M31 has had a more active recent accretion history than that of the Milky Way (Font et al. 2006b; Fardal et al. 2006, 2007; Brown et al. 2006, 2008; McConnachie et al. 2009). The halo of the Milky Way has a power-law density profile with exponent $2 < \gamma < 4,$ and an estimated oblateness of $0.5 < c/a < 0.8$ (see, e.g., Newberg & Yanny 2005; Bell et al. 2008; Jurić et al. 2008). The halo of M31 has been characterized with a power-law surface brightness profile of exponent $\gamma \sim 2$ (Guhathakurta et al. 2005; Ibata et al. 2007; Courteau et al. 2011) and it contributes $\sim 4\%$ of the total luminosity of M31 out to 200 kpc along the minor axis (Courteau et al. 2011). Given the stochasticity involved in the process of stellar halo formation, it is important to enlarge the sample of observed galactic halos to differentiate between the models and quantify model predictions from galaxy to galaxy.

The GHOSTS (Galaxy Halos, Outer disks, Substructure, Thick disks, and Star clusters) survey (PI: R. de Jong) is the largest study of resolved stellar populations in the outer disk and halos of 14 nearby disk galaxies to date.[6] A detailed description of the survey can be found in Radburn-Smith et al. (2011, hereafter R-S11). Briefly, the targeted galaxies are imaged with the Advanced Camera for Surveys (ACS) on board *HST* and their individual stars are resolved. GHOSTS observations provide star counts and CMDs typically 2–3 mag below the tip of the RGB (TRGB) of the outer disk and halo of each galaxy. Such data allow us to shed light on various issues. For instance, using the RGB stars as tracers of the faint underlying population, we are able to study the size and shape of each stellar halo. In addition, we can constrain their stellar properties, such as age and metallicity. These observations can then be used to help distinguish between models for the formation of spiral galaxies.

Among the galaxies observed by the GHOSTS survey, M81 (NGC 3031) is of particular interest. It is the nearest massive spiral galaxy with similar global properties to the Milky Way and M31, and it contains the largest number of fields observed within the survey. These observations probe different regions of M81's halo out to large galactocentric distances, enabling us to investigate whether stellar population variations and/or metallicity gradients are found in this galaxy. The farthest field observed in M81 is at a projected distance of ~ 50 kpc from the galactic center along the minor axis, an unprecedented distance for halo studies outside the Local Group. M81 thus provides a key laboratory to study the stellar properties of halos of massive spiral galaxies outside the Local Group and to test model predictions.

Tikhonov et al. (2005) used archival *HST*/WFPC2 observations of M81 to study the spatial distribution of its asymptotic giant branch (AGB) and RGB stars. They suggested that the transition from a disk-dominated to a halo-dominated population occurs at a deprojected distance of ~ 20 kpc. Later *HST* studies of the resolved stellar populations of fields closer than ~ 20 kpc show CMDs exhibiting relatively young stars and older RGB stars with a wide range in metallicity (Williams et al.

---

6 http://archive.stsci.edu/prepds/ghosts

2009). These stars likely belong to the disk of M81. Mouhcine et al. (2005b) have studied the metallicity of RGB stars observed with a WFPC2 *HST* field located at a projected distance of ~15 kpc from the galactic center. They found a mean metallicity of [Fe/H] ~ −1.25 dex assuming an age of 12 Gyr, more metal-poor than the metallicity inferred from closer fields, indicating that these are halo stars. Barker et al. (2009, hereafter B09) analyzed the outskirts of the northern half of M81 from a wide-field study of resolved stellar populations using the Suprime-Cam instrument on the 8 m Subaru telescope and covering an area ~0°.3. They found a flattening of the stellar density profile beyond a deprojected distance of 18 kpc (at approximately 6 scale lengths, being M81's disk scale length ≈2.7 kpc) with stars of metallicities [Fe/H] ~ −1.1 ± 0.3 dex, assuming a 10 Gyr old age. B09 discussed the possibility that this represents the underlying stellar halo of M81. This outer component is more metal-poor than the stars found in the interior region of their field, again suggesting that M81's faint, extended component starts to dominate at about $R_{dp} \sim 20$ kpc. B09 find that its RGB stars follow a power-law surface density profile with an exponent of $\gamma \sim 2$, similar to the halo density profile of both the Milky Way and M31. They moreover estimate that this component would contain ~10%–15% of M81's total *V*-band luminosity, several times more luminous than both the Milky Way's and M31's halo, although the systematic uncertainty in this estimate is about ±50% due to uncertainties in the diffuse light sky subtraction within 14–18 arcmin. The only age estimate for the halo of M81 from its resolved stellar population was reported by Durrell et al. (2010), who analyzed very deep observations of one *HST*/ACS field at ~19 kpc from the center of M81. From fits to the red clump (RC), RGB, and RGB bump, they estimated a mean age for the dominant population of 9 ± 2 Gyr. They also found that the metallicity distribution function peaks at [Fe/H] = −1.15 ± 0.11 dex.

M81 has had an active recent interaction history. H I gas surrounding M81, M82, and NGC 3077 show filamentary structures (van der Hulst 1979; Yun et al. 1994) that can be explained as the result of tidal interactions among all three galaxies, probably ≈200–300 Myr ago (Yun 1999). In addition, recent star formation activity has been observed in the most prominent H I filaments, e.g., Arp's Loop and Holmerg IX (de Mello et al. 2008; Sabbi et al. 2008; Weisz et al. 2008; Mouhcine & Ibata 2009) as well as in the outskirts of M81, especially in the H I bridge connecting M81 and NGC 3077 (Mouhcine & Ibata 2009). It has been suggested that these may be new tidal dwarf galaxies, forming out of the gas stripped from the interacting galaxies (de Mello et al. 2008; Sabbi et al. 2008; Weisz et al. 2008; Mouhcine & Ibata 2009). Using the MegaCam imager on Canada–France–Hawaii Telescope, Mouhcine & Ibata (2009) presented a panoramic view of M81, which covers the entire galaxy and the southeast outskirts, including the most prominent H I filaments and NGC 3077. They found new young stellar clumps, whose properties can also be best explained if these systems are of tidal origin.

In this paper, we analyze the stellar populations of M81's halo stars by studying the color distribution of a sample of 19 fields near M81. We compare our observations with predictions from models of stellar halo formation. A companion paper (M. Vlajić et al., in preparation) will present the minor and major axis halo density profiles of M81 as traced by the RGB stars observed. The paper is outlined as follows. The observations and photometry are presented in Section 2. Analysis of the CMDs and color distributions of the M81 fields are in Sections 3 and 4,
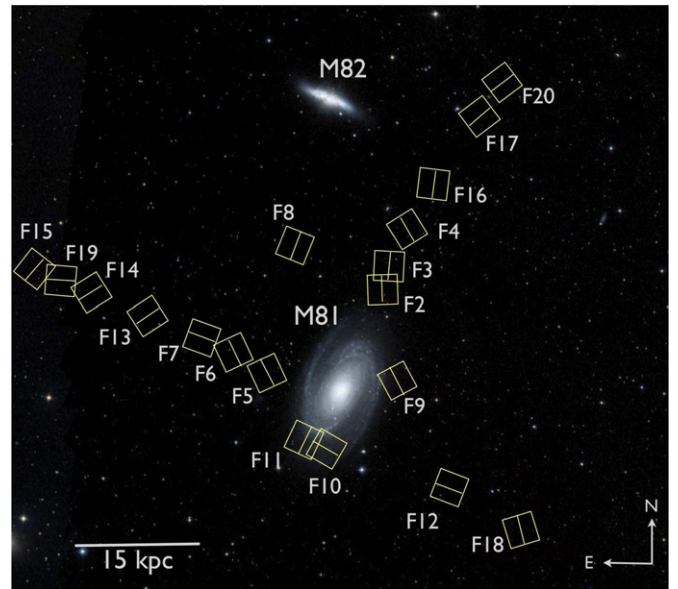

Figure 1. DSS colored image of M81 showing the location of the 19 *HST* ACS/WFC fields used in this work. North is up and east is to the left. Fields F2–F12 were already introduced in R-S11 whereas fields F13–F20 are new observations. The image is ~1°.25 × 1°.25. Each ACS field of view (FOV) covers a region of ~3.6 × 3.6 kpc² on the sky at the distance of M81 (3.6 Mpc, R-S11), and has a pixel scale of 0″.05. Information about these observations can be found in Table 1. The satellite galaxy M82 can also be seen.

respectively. Section 5 introduces the method used to transform the model stellar particles into CMDs. A comparison of our observations with models of stellar halos formed entirely from accreted objects is presented in Section 6. We discuss our results in Section 7 and conclude in Section 8.

All throughout the paper we use the term "M81's halo" to refer to stars located at projected distances $R > 15.5$ kpc from the center of M81. This is the region where the faint, extended R^{-2} structural component detected by B09 starts to dominate, at ≈6 disk's scale lengths. We adopt a distance modulus for M81 of $(m − M)_0 = 27.79$ (R-S11), which is in agreement with previous values for the distance modulus of M81, e.g., $(m − M)_0 = 27.75 ± 0.08$ (Freedman et al. 2001), $(m − M)_0 = 27.78 ± 0.05$ (McCommas et al. 2009), $(m − M)_0 = 27.78 ± 0.04$ (Dalcanton et al. 2009), and $(m − M)_0 = 27.86 ± 0.06$ (Durrell et al. 2010).

2. OBSERVATIONS AND PHOTOMETRY

We use *HST* ACS/WFC images in the *F*606*W* and *F*814*W* filters of 19 fields near M81 from the GHOSTS survey (see R-S11). As shown in Figure 1, most of the pointings are spaced along the minor and major axes of M81 mainly to measure its halo structure (M. Vlajić et al., in preparation). This strategy allows us to probe the halo of M81 out to a projected distance of $R \sim 50$ kpc from the galactic center, an unprecedented distance for halo studies outside the Local Group. Fields 2–12 were introduced in R-S11, while Fields 13–20 are new observations obtained in our Cycle 17 SNAP program (M. Vlajić et al., in preparation). A summary of the GHOSTS fields used in this work can be found in Table 1.

Stellar photometry was performed using DOLPHOT, a modified version of HSTPHOT (Dolphin 2000) for ACS images. We refer the reader to R-S11 for full details of the GHOSTS data pipeline developed for the photometric reduction. Briefly,

Table 1
M81 *HST*/ACS Observations

Field[a]	Proposal ID	Proposal PI	α_{2000} (h m s)	δ_{2000} (° ′ ″)	Observation Date	t^{b}_{F606W} (s)	t^{b}_{F814W} (s)	$E(B-V)^{c}$	R^{d} (kpc)
F02	10915	Dalcanton	09 54 34.71	69 16 49.76	2006 Nov 16	24232 (10)	29953 (12)	0.086	15.0
F03	10523	de Jong	09 54 23.12	69 19 56.41	2005 Dec 6	730 (2)	730 (2)	0.090	18.5
F04	10523	de Jong	09 53 59.63	69 24 58.57	2005 Oct 26	695 (2)	695 (2)	0.089	24.4
F05	10523	de Jong	09 57 17.23	69 06 29.27	2005 Oct 31	700 (2)	700 (2)	0.079	10.4
F06	10523	de Jong	09 58 04.50	69 08 52.15	2005 Oct 31	700 (2)	700 (2)	0.077	15.5
F07	10523	de Jong	09 58 52.30	69 10 42.12	2005 Sep 7	720 (2)	720 (2)	0.071	20.5
F08	10523	de Jong	09 56 39.13	69 22 29.58	2005 Dec 20	740 (2)	740 (2)	0.078	21.0
F09	10136	Bond	09 54 16.54	69 05 35.71	2005 Apr 13	5354 (4)	5501 (4)	0.080	7.6
F10	10584	Zezas	09 56 29.23	68 54 42.49	2005 Dec 9	1580 (3)	1595 (3)	0.078	11.3
F11	10584	Zezas	09 57 01.91	68 55 56.29	2005 Dec 6	1580 (3)	1595 (3)	0.078	12.0
F12	10604	Sarajedini	09 53 03.20	68 52 03.60	2005 Sep 11	12470 (10)	22446 (18)	0.074	19.3
F13	11613	de Jong	10 00 14.30	69 13 14.75	2010 Jan 18	850 (2)	690 (2)	0.065	29.0
F14	11613	de Jong	10 01 34.88	69 16 03.11	2010 Jul 22	850 (2)	690 (2)	0.062	37.0
F15	11613	de Jong	10 02 56.42	69 18 53.08	2010 Jan 23	850 (2)	690 (2)	0.057	45.5
F16	11613	de Jong	09 53 20.88	69 30 30.71	2010 Jun 3	850 (2)	690 (2)	0.091	31.3
F17	11613	de Jong	09 52 13.33	69 38 59.17	2010 Jul 16	850 (2)	690 (2)	0.098	42.3
F18	11613	de Jong	09 51 23.91	68 46 29.97	2009 Nov 9	850 (2)	690 (2)	0.074	30.4
F19	11613	de Jong	10 02 15.46	69 17 33.68	2010 Feb 25	830 (2)	680 (2)	0.059	41.4
F20	11613	de Jong	09 51 41.10	69 43 14.85	2009 Dec 31	830 (2)	680 (2)	0.094	47.9

Notes.
[a] Field number. Fields 2–12 were presented in R-S11 and are labeled following their notation. Fields 13–20 are new observations from our Cycle 17 program.
[b] Total time of exposure time. The number of exposures in each filter is indicated in brackets.
[c] Reddening values estimated by Schlegel et al. (1998). Note that, as stated in the text, we calculate the extinction for each bandpass using the corrected extinction ratios by Schlafly & Finkbeiner (2011), which recalibrate the Schlegel et al. (1998) dust maps.
[d] Projected distance from the galactic center, without taking into account M81's inclination.

DOLPHOT performs point-spread function fitting on all the flat-fielded images per field simultaneously. The DOLPHOT parameters used for performing photometry on the GHOSTS fields are similar to those used in the ACS Nearby Galaxy Survey Treasury (ANGST) program (Dalcanton et al. 2009). The final output of DOLPHOT provides both instrumental VEGA and transformed Johnson–Cousins magnitudes already corrected for charge transfer efficiency (CTE) loss and with aperture corrections calculated using isolated stars. CTE correction is applied by DOLPHOT to each source detected using the analytical formulae provided by Chiaberge et al. (2009). The photometric output also includes various diagnostic parameters that can be used to discriminate spurious detections from the actual stars. Contamination from Galactic foreground stars was estimated using the Besançon model (Robin et al. 2003). We find that only ∼50 foreground stars are expected per ACS field. The most important source of contamination in these fields are unresolved background galaxies. The estimated galaxy density was obtained using the GalaxyCount program (Ellis & Bland-Hawthorn 2007) and it is 22, 55, 121, and 240 arcmin^{-2} at $F814W = 24$, 25, 26, and 27 mag, respectively. Several selection criteria to discriminate unresolved galaxies from stars were optimized using deep archival high-redshift *HST*/ACS fields. These were applied to the raw photometric output, which removed ∼95% of the contaminants. Details on the photometric culls and how they were optimized can be found in R-S11. In addition, a mask of all extended and resolved objects was constructed for each field using SEXTRACTOR (Bertin & Arnouts 1996). Detections lying in the pixel positions of the masked sources were discarded from the star catalog.

Extensive artificial star tests (ASTs) were performed in both filters of all images to assess the completeness level and quantify the photometric errors of the data. The procedure of the ASTs is explained in detail in R-S11. In short, approximately 2,000,000 artificial stars per field in both filters are injected and photometered by DOLPHOT, one at a time to avoid affecting the image crowding. The artificial stars were distributed according to the observed stellar gradient, thus the higher surface brightness regions of an observation were populated with more artificial stars. The colors and magnitudes of the injected artificial stars are realistic and they cover not only the observed values but also fainter magnitudes to explore the possibility of recovering a faint, unresolvable star. We applied the same cull as in the real images. Artificial stars that did not pass the cull were considered to be lost. The completeness level was calculated as the ratio of recovered-to-injected number of artificial stars at a given color and magnitude bin. The 50% completeness level varies from field to field but it is typically found at $F814W \sim 26$, which is approximately 2 mag fainter than the TRGB, measured to be located at $F814W \sim 23.7$ for M81 (R-S11). The 50% completeness level appears to be rather color independent for most regions of the CMD. For colors $(F606W - F814W) \gtrsim 1.7$, or equivalently $F606W \gtrsim 27.5$, however, the incompleteness is more severe (see Figure 2).

3. THE COLOR–MAGNITUDE DIAGRAMS OF THE M81 FIELDS

Figure 2 shows the CMDs of stars for each field, after the culling and masks were applied. The magnitudes have been corrected for Galactic extinction using the corrected extinction ratios $A_{\lambda}/E(B-V)$ of 2.47 and 1.53 for $F606W$ and $F814W$, respectively, that are to be used with the $E(B-V)$ values from Schlegel et al. (1998) dust maps and the $R_V = 3.1$ extinction law (Schlafly & Finkbeiner 2011). Given the variable Galactic extinction across the sampled region of M81, each field was corrected with its appropriate $E(B-V)$ value as listed in Table 1, with a total range of 0.05–0.1. The 50% completeness level of
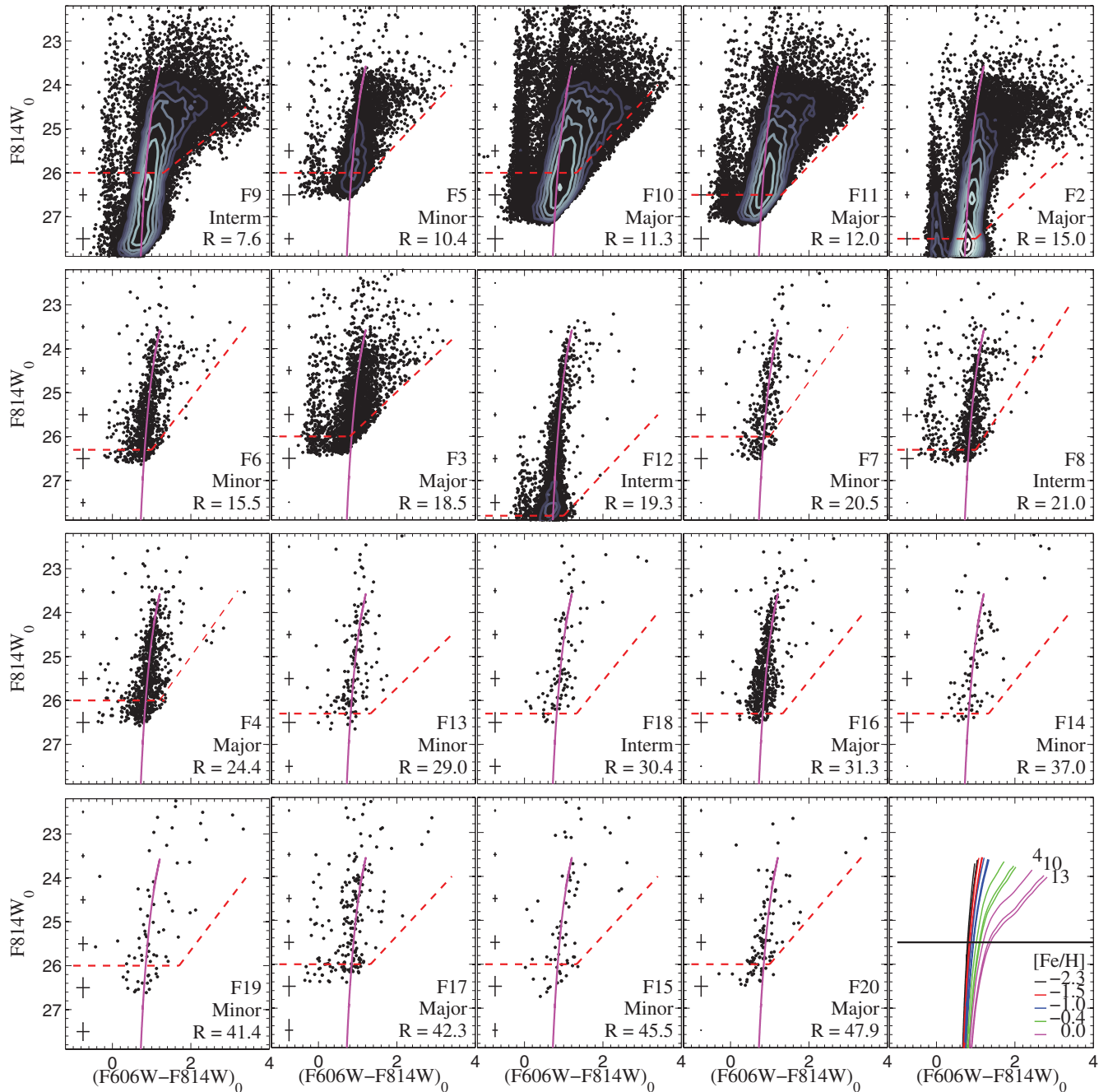
Figure 2. CMDs of the 19 ACS/WFC fields in M81 after correcting for extinction and reddening. We show only the stars that remain after the culling and masks were applied to the DOLPHOT photometric outputs. At densities greater than 40 stars in a 0.1×0.14 bin in color and $F814W$, a Hess diagram is shown with contours at 40, 60, 100, 160, 250, 400, 650, and 1000 stars per 0.014 mag^2. Magnitudes are calibrated onto the VEGAmag *HST* system and corrected for Galactic extinction (see Table 1). Labels "Major," "Minor," and "Interm" indicate that the field is located on the major, minor or on intermediate axis, respectively. The projected distance, R, of each field from the center of M81 is indicated in units of kpc. A 10 Gyr old, [Fe/H] = -1.2 dex isochrone from the BaSTI library Pietrinferni et al. (2004) is superposed in each panel. Red dashed lines indicate the 50% completeness level as determined from the ASTs. The photometric errors are also obtained from the ASTs and refer only to color ($F606W - F814W$) = 1. The rightmost bottom panel shows, with different colors, BaSTI isochrones covering a grid of metallicities for three different ages: 4, 10, and 13 Gyr from left to right of each color which indicate the age–metallicity degeneracy present in the RGBs. Old and more metal-poor populations resemble younger and more metal-rich ones. The black solid horizontal line shows the limiting magnitude that we used for the color analysis performed in the following sections.

(A color version of this figure is available in the online journal.)

each field as well as their projected radial distance from the center of M81 is indicated in each corresponding panel. The stellar density tends to decrease with increasing galactocentric radius, as expected. We note that the projected distances were calculated using circular symmetry, without taking into account M81's inclination. Therefore, due to the elliptical symmetry of the disk's density profile, fields located at similar projected

distances but lying on different axes will have different stellar densities.

The CMDs are mostly populated by old RGB stars (older than 1 Gyr). Note, however, that signs of younger populations such as blue, extended MS stars(<500 Myr) or massive stars burning helium in their core (25–600 Myr old red and blue loop sequence stars) appear primarily in the fields closer than

$R \sim 15$ kpc, which are dominated by disk stars. In this work, we focus on the stellar populations of M81 fields located at $R > 15$ kpc (≈ 6 disk's scale lengths), where the faint extended R^{-2} structural component detected by B09 starts to dominate. A flattening in the surface brightness profile is also detected using the resolved stars of our GHOSTS fields at $R \sim 18$ kpc (M. Vlajić et al., in preparation). We detect the faint structural component discovered by B09 out to a larger projected radius, $R \sim 50$ kpc, and we refer to it hereafter as *M81's halo*. Although it is not yet clear what the nature of this structural component is (see discussion in B09), we will assume that it is the halo of M81 when comparing with predictions by models of galaxy formation (see Section 6). We can gain some insight about the halo's dominant population by fitting isochrones to the RGBs of their CMDs. We find that a BaSTI isochrone (Pietrinferni et al. 2004) of 10 Gyr with metallicity [Fe/H] = -1.2 dex matches reasonably well the shape of the RGB, as shown in Figure 2. This is consistent with the results by Durrell et al. (2010), who derived a mean metallicity of [M/H] = -1.15 ± 0.11 dex and an age of 9 ± 2 Gyr from the shape of the RGB, the magnitude of the RC, and the location of the RGB bump of one of the fields (F12) also analyzed in this work.

We note that fields F14 and F15 have RGBs slightly redder than the isochrone superposed in Figure 2. This might suggest that the halo populations in such fields have metallicities higher than [Fe/H] = -1.2 dex. In fact, their RGBs can also be well fitted with a 10 Gyr isochrone of metallicity [Fe/H] = -1 dex. The redder RGBs might indicate the presence of substructure dominating these fields that we might be unable to clearly observe due to pencil-beam nature of our survey. However, calibration uncertainties due to, e.g., CTE correction uncertainties between chips, flat field (Dalcanton et al. 2012), or different roll angles can account for up to ~ 0.05 mag uncertainty in color. This uncertainty was determined by comparing the median colors of overlapping stars in fields F2–F3, F10–F11 in M81, as well as in other fields of the GHOSTS survey (see R-S11). Therefore, it is unclear whether the difference in colors is related to metallicity variations in these fields.

On the other hand, fields F8 and F17 have very bright and blue MS stars at projected distances of 21 kpc and 42.3 kpc, respectively, quite far away from the disk of M81. This is more likely related to the H I gas that surrounds M81, M82, and NGC 3077 and show filamentary structures (Yun et al. 1994) that can be explained as a consequence of close encounters between M81 and its two neighbors about 200–300 Myr ago (Yun 1999). F8 is located in the region of the H I tidal bridge connecting M81 and M82, called Arp's loop. F17 is also superposed on H I gas detected in the system. Previous works have suggested that the bright young stars in the Arp's loop may have formed in the gas stripped from these interacting galaxies (de Mello et al. 2008) and studies of a wide-field imaging of the northern half-region of M81 show that the surface density of young stars ($\lesssim 100$ Myr) traces the H I column density observed (B09). A similar scenario could explain the presence of young stars in F17. Finally, field F3 is located at $R > 15$ kpc and it also contains very young main-sequence stars, as well as bright AGB stars above the TRGB. However, since it lies on the major axis of M81's disk, it is expected to contain a larger contribution of disk stars than a minor axis field at a similar projected distance from the galactic center (e.g., F12). In addition, F3 is located on a high column density of H I as detected by Yun et al. (1994).

We also note that fields F16, F17, and F20 are relatively close, in projected distance, to M82 (see Figure 1). To investigate whether there is a significant contribution from M82's halo stars in them, we inspected the density distribution of stars in the outer areas of this galaxy using ANGST data (Dalcanton et al. 2009). The data cover the entire disk of M82 and to some extent the outer regions, being the outermost field at ~ 3.5 kpc from M82's center. We find that there is a factor of ~ 20 more stars in M81 than in M82 at a 3.5 kpc projected distance from each galaxy. If we assume that the stellar density difference remains the same out to larger distances, we can use the observed stellar density profile of M81 (see M. Vlajić et al., in preparation) and estimate the corresponding density of M82's stars at 22 kpc, which is the projected distance of F20 from M82's center. We obtain that the number of M82's stars at 22 kpc is $\sim 1/3$ of what is observed in field F20.[7] We emphasize that this estimate is extremely uncertain; an R^{-2}-power-law fit to the stellar density distributions would estimate a factor of ~ 5 lower contribution from M82 than from M81 at the location of F20. In addition, as we show in the next section, we see no differences in colors in the fields closest to M82. We therefore assume that the results presented below are not significantly influenced by M82's halo.

4. THE COLOR DISTRIBUTION OF M81's HALO

As shown in Figure 2, we mostly observe stars populating the RGB in the halo CMDs of M81. Because the age and metallicity are partially degenerate in this evolutionary phase (see, e.g., Worthey 1994), it is impossible to constrain the ages and metallicities of the stars from these CMDs alone. However, the effects of age are relatively small compared to metallicity, such that the color of the RGB is an approximate indicator of metallicity. Here we analyze the colors of the RGBs as a function of galactocentric distance, which will then be directly compared with predictions by models of galaxy formation (see Section 6).

In order to obtain a distribution that better reflects the spread in metallicity on a given observed field, we define a new color index Q by slightly rotating the CMDs an angle of $-8°.29$, where a line of slope -6.7 becomes vertical. The rotation is such that the magnitude axis (y-axis) of each CMD is parallel to the [Fe/H] = -1.2 dex isochrone shown in Figure 2, which represents well the RGB of the halo fields. Figure 3 shows the normalized Q color function (CF) distributions for each field, plotted as black dots in bins of $\Delta Q = 0.3$. The error bars simply indicate Poisson noise. The field number and the projected radial distance from the center of M81 in kpc are indicated in each panel. The CFs are calculated using stars within the magnitude range $23.7 \leqslant F814W \leqslant 25.5$. The lower magnitude limit ensures that stars are brighter than the 50% completeness level in all the fields and have small photometric errors, while the upper magnitude limit corresponds to approximately the TRGB magnitude and thus minimizes contamination from bright AGB stars or other contaminants. The rightmost bottom panel in Figure 3 shows both the line parallel to the isochrone (green line) as well as the magnitude range considered (within the magenta lines) to construct the CFs for one of the observed CMDs (field F13).

The widths of the CFs, which provide an idea of the range in colors at any given radius, vary from field to field. The CFs become generally narrower as we get farther out from

---

[7] We obtain a similar result if we consider the distance and stellar density of field F17. Field F16, on the other hand, has a factor of four more stars than that expected from M82's halo.
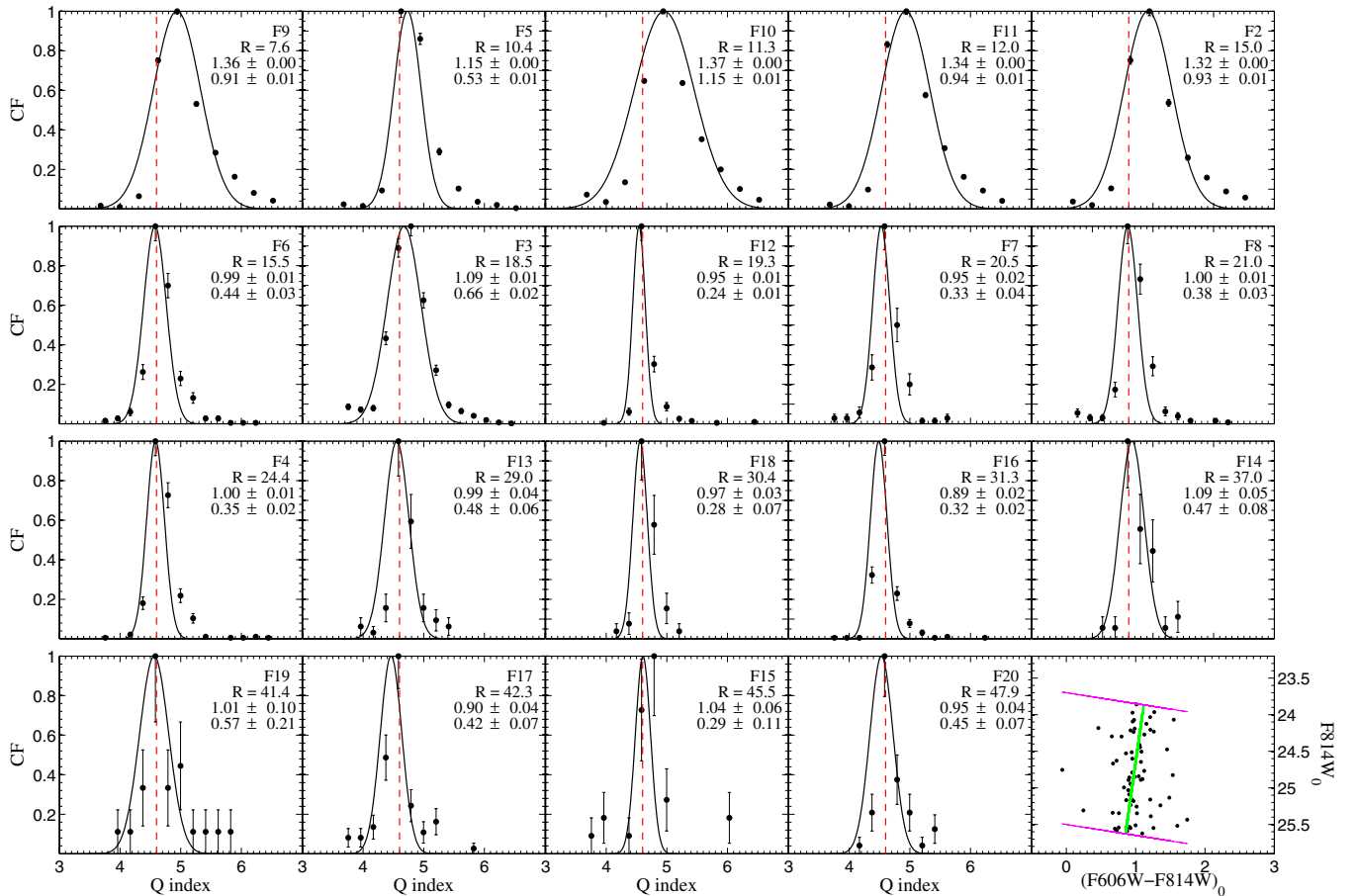
Figure 3. Color function (CF) distribution of each field of M81. Only stars within the magnitude range $23.7 \leqslant F814W \leqslant 25.5$ were considered to build the CFs, as shown in the rightmost bottom panel. Black dots show the Q-color distribution of stars, which were divided into 15 bins in the color index Q range $3.5 \leqslant Q \leqslant 6$, and normalized to one. Error bars to the data points are simply Poisson noise. The field number and its projected radial distance, R, from M81's center in kpc are indicated. The values below the radius correspond to the median of the ($F606W - F814W$) color and its corresponding uncertainty, and the width of the CF and its uncertainty is written below it. The width of each CF was calculated from a Gaussian function, shown here as a solid line, which was obtained from fitting the entire data (not the binned data) using a maximum likelihood method. Note that the median of the color becomes bluer as we get farther from the galactic center. Also the width appears to mostly become smaller at larger galactocentric distances. The dashed red line in each panel is at the same Q value in all the plots to help visualize differences in the CFs among the fields. The rightmost bottom panel shows the CMD of field F13 with a green line superimposed. This line is parallel to the isochrone shown in Figure 2 which was used as the new y-axis to define the Q index. The length of the line, as well as the magenta lines, indicates the range of magnitudes considered in this analysis.

(A color version of this figure is available in the online journal.)

the galactic center. To quantify the CF widths, we fitted a Gaussian function to the Q color distribution of each field using a maximum likelihood method.[8] We iteratively rejected 3σ outliers to avoid fitting the tails of the distributions. Since the CMDs have different depths, we took into account the photometric errors on the individual data points when fitting the Gaussians, in order to avoid introducing systematic errors on the CF widths. The resultant intrinsic CF widths were calculated as the FWHM of each Gaussian distribution, plotted as a solid line in Figure 3. The median ($F606W - F814W$) colors, obtained by rotating the median Q to the original axes, as well as the CF widths are indicated in Figure 3. The median ($F606W - F814W$) colors are associated with the median magnitudes of the stars used in the Gaussian fits. Uncertainties in the maximum likelihood estimates of both the median colors and widths are also indicated and take into account Poisson counting uncertainties and photometric errors. As shown in Figure 2, the photometric incompleteness affects the reddest regions of the

CMDs ($F606W - F814W \gtrsim 1.8$) almost exclusively in the inner fields. However, the number of stars in the red end is rather low compared with the number of stars in the entire CMD, therefore we do not expect this to be a big concern in our analysis. At most, a correction for this effect would yield to slightly redder median colors for the inner fields.

These results are better illustrated in Figure 4. The top panel shows the median ($F606W - F814W$) colors as a function of galactocentric distance. Black dots represent the values obtained for the observed CMDs. The error bars show the median color uncertainties. Red circles around black dots highlight fields lying on the major axis of M81. There is a sharp jump in the observed colors at $R \sim 15.5$ kpc. Fields closer than $R \sim 15.5$ kpc from the center of M81 show a significantly redder ($F606W - F814W$) color, ~1.35 mag, than those located at farther distances, color ~1.0 mag. One exception is F5, which is closer than 15 kpc but exhibits a color similar to that of fields farther out. Since F5 is located on the minor axis of M81, its populations are less disk-dominated than fields whose projected distances are similar but lie on the major axis of M81, e.g., F10 and F11.

---

[8] Note that the parameters of the Gaussian function are estimated from all the data points and not from the binned data.
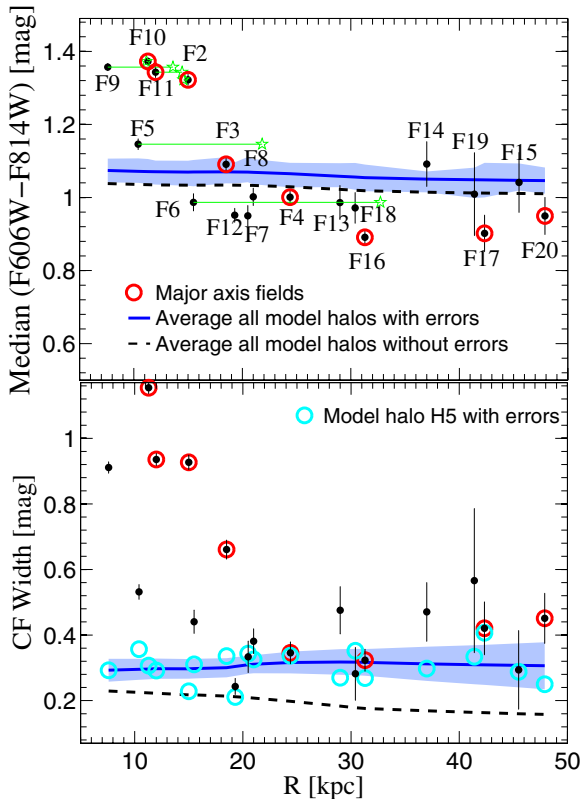
Figure 4. Top panel: median color profiles. Black dots indicate this value for the M81 observations as a function of projected distances R to the galactic center. The error bars indicate the median uncertainty. Red circles around black dots highlight fields located on the major axis of M81. Green stars indicate the deprojected distances of fields within $R < 15.5$ kpc. The colors of these fields (F2, F5, F6, F9, F10, F11) decrease with increasing major-axis distance (see the text), which supports the idea that these fields are mostly dominated by disk stars. Thus, assuming that fields located at projected distances $R > 15.5$ kpc are pure halo populations, *we do not detect any color gradient in the halo of M81*. The average color profile of the 11 smooth halo components of the models analyzed (see Section 5) is shown as a blue solid line and the shaded area indicates the 1σ model-to-model deviations from the average. Both observations and models lack a color gradient. The dashed black line is the average color profile of the model fields, before the observational effects were simulated, as explained in Section 5. Bottom panel: widths of the CFs as a function of projected galactocentric distance. The observed M81's fields show a broader CF at $R < 15$ kpc and a smaller range in colors for fields further out. The widths obtained for the models agree with those for observed fields at $R > 15$ kpc. Again the dashed black line shows the average widths for the model CFs before the observational effects were simulated. Cyan open circles show the widths as a function of radius for one halo model, H5. See the text for more details.

(A color version of this figure is available in the online journal.)

In general, the jump in the observed colors is likely due to the contribution from disk stars, which becomes negligible outside $R = 15.5$ kpc, although we cannot rule out the possibility that some of the stars at $R < 15.5$ kpc might have higher scale height than the disk.[9] To explore the nature of the stars in fields at $R < 15$ kpc, we use the ellipticity of M81's disk, assuming an inclination of 62°.7 and a position angle of 157°, as listed in HyperLeda[10] (Paturel et al. 2003), to generate ellipses passing through the inner fields and calculate their deprojected distances. Green stars in the top panel of Figure 4 indicate those ellipses' semimajor axes length. The colors of these fields (F2, F5, F6, F9, F10, F11) decrease with increasing semimajor axis

---
[9]   Observations of more edge on galaxies will help to understand better halo flattening, and how it changes with radius.
[10]   http://leda.univ-lyon1.fr/

distance, which is consistent with the idea that they follow the disk's ellipticity and thus are mostly dominated by disk stars.

Assuming that fields at projected distances $R > 15$ kpc are pure halo populations, i.e., belonging to the extended R^{-2} structural component detected by B09 as well as in the GHOSTS fields (M. Vlajić et al., in preparation), an interesting result from Figure 4 is that *no sign of a color gradient is observed in the halo of M81*. We detect, nevertheless, a small degree of scatter in the median color of 0.055 mag root mean square (rms). However, as briefly mentioned in Section 3, there are uncertainties due to the star's image position that are not reflected in the photometric uncertainties, both from DOLPHOT and ASTs. These uncertainties are possibly due to CTE corrections between chips, errors in the flat field (Dalcanton et al. 2012), or differences in the roll angle, and have been tested using overlapping stars of three *HST*/ACS fields within the GHOSTS survey (see R-S11). The mean instrumental uncertainty in ($F606W - F814W$) colors is ∼0.05 mag. Thus, the level of variation detected is consistent with being due to (mainly) systematic and random errors. Therefore, we are incapable of distinguishing whether the scatter in color is physical, indicating real age/metallicity variations, or instrumental. On the other hand, if we consider the possibility of a color gradient in M81's halo, a linear fit to the colors of fields farther than 15 kpc from M81's center yields a slope (or color gradient) of -0.0009 ± 0.0031 mag kpc^{-1} with a significant scatter around the median color–distance relation, with $\sigma \sim 0.056$ mag. This is consistent with no color gradient. Using the obtained slope, we can place a limit of 0.03 ± 0.11 mag difference between the median color of RGB halo stars at ∼15 and at 50 kpc, corresponding to a difference of 0.08 ± 0.35 dex in [Fe/H] over that radial range, for an assumed age of 10 Gyr.

The bottom panel of Figure 4 shows the CF widths as a function of galactocentric distance. We find that there is also a jump in the observed widths, such that fields closer than 15 kpc have broader CFs than those located farther away. The uncertainties in the widths are larger at increasing radius, due to the small number of stars found at large galactocentric distances. The color distribution width of ∼0.4 mag for the fields at $R > 15$ kpc suggests that the halo fields possess a spread in metallicity, in spite of the observational effects. We discuss the possible spread in metallicity and return to this figure in general later in the next section, when we compare these results with halo model predictions. We have also measured the color profile using only stars closer to the TRGB, within the magnitude range $23.6 \leqslant F814W \leqslant 24.3$, where there is a more sensitive color variation, but much fewer stars. The results that we obtain remain overall the same, except that the median colors of each field become redder. In addition, the jump observed between the colors at $R \sim 15$ kpc increases when considering only stars near the TRGB, as the median colors of fields at $R < 15$ change by ∼0.35 mag with respect to the colors shown in Figure 4, whereas this change for fields at larger radii is smaller, ∼0.15 mag.

We note that the median colors of the RGB stars in regions where the H I filaments have been found (Yun et al. 1994), mainly fields F3, F5, and F8, are not peculiar with respect to the ones elsewhere in the outskirts of M81. These fields do contain main-sequence stars, i.e., evidence of younger populations, in comparison with fields at similar distances but lying outside the H I filaments. Our results thus suggest that the recent interactions among M81, M82, and NGC 3077 have little influence on the RGB old stars distribution. On the other hand, fields F17 and F20 might have contributions from M82 and the determination

of their median colors might be more uncertain. They are located at ~20 kpc from M82 whereas their distance from M81 is ~45 kpc. However, M81 is a much larger and massive galaxy and therefore its contribution to fields F17 and F20 is expected to be more than that of M82. We estimated that the M82's contribution could be ~1/3 in these fields, but this is highly uncertain (see the last paragraph of Section 3.)

In summary, we can characterize the RGB of the halo of M81 by a color distribution of width ~0.4 mag and approximately constant median value of $(F606W - F814W) \sim 1$ mag with variations of 0.055 mag rms, over a range of $15 \leqslant R \leqslant 50$ kpc. The intrinsic color variation is <0.055 mag, which is consistent with being due to random and systematic error alone. When considering the possibility of a color gradient, we find a limit of 0.03 ± 0.11 mag difference between the median color of RGB halo stars at ~15 and at 50 kpc, which corresponds to a difference of 0.08 ± 0.35 dex in [Fe/H] over that radial range.

5. STELLAR HALO MODELS: FROM STAR PARTICLES TO CMDs

To compare the properties of the observed stars with models of galaxy formation, we use the set of stellar halo models presented by Bullock & Johnston (2005, hereafter BJ05) and construct CMDs of ACS-like fields. These stellar halos are formed by the pure accretion of satellite galaxies within a ΛCDM cosmology. Full details about these cosmologically motivated simulations can be found in previous works (BJ05; Robertson et al. 2005; Font et al. 2006a). Here we provide a brief summary of their main characteristics.

To determine the accretion history of each galactic halo, a merger tree is generated using the extended Press–Schechter formalism (Lacey & Cole 1993). A self-consistent *N*-body simulation follows the dynamical evolution of the dark matter component of the accreted satellites, which are being disrupted within an analytic, time-dependent halo+disk potential. A cosmologically motivated semianalytic formalism is used to both follow the gas accretion history of each satellite and model its star formation rate. Star formation is truncated soon after each satellite falls into the main halo potential, when the gas is assumed to be lost due to ram pressure stripping (see, e.g., Lin & Faber 1983; Mayer et al. 2006). The stellar components of each satellite are associated with the more tightly bound dark matter particles in the halo, which are assigned a radially dependent mass-to-light ratio that produces a reasonable light profile for the model satellites. The chemical evolution of each satellite is modeled with the method of Robertson et al. (2005), which takes into account the enrichment from both Type II and Type I supernovae.

BJ05 performed 11 halo realizations. They reproduce several observed properties of the Milky Way surviving satellites, such as their luminosity function (LF), the luminosity–velocity dispersion relation, and their surface brightness distribution. The final stellar halo luminosities are comparable to the estimated total luminosity for the stellar halo of the Milky Way. It is worth noting that the luminosities as well as other properties of the stellar halo realizations span a certain range such that these models are also suitable for comparing the halo properties of M81, whose luminosity and mass are similar to those of the Milky Way (see, e.g., Karachentsev 2005). Differences among the 11 realizations are purely due to differences in the model accretion history. The publicly available outputs of the

simulations[11] provide, among other things, ages, metallicities, and masses of the stellar populations associated with particles that make up a Milky Way like halo at redshift $z = 0$. For the analysis below, we only consider the smooth component of each stellar halo model, thus neglecting stellar populations that belong to surviving satellites, i.e., stellar particles that are still gravitationally bound to their original progenitor (see BJ05). We refer to each halo model as H1, H2, ..., H11.

We rotate the models by 60° around the *X* axis, to simulate M81's inclination, and generate ACS-like fields with particles located within 5–50 kpc, resembling the locations of our GHOSTS fields. For each of the mock fields, we construct a stellar "mock-CMD" containing the predicted mixture of stellar populations as follows.

1. We first grid the total range of ages and metallicities available in the full halo model ($2 \leqslant$ age $\leqslant 13$ Gyr and $-4 \leqslant$ [Fe/H] $\leqslant -0.4$ dex) with a regular mesh of bin size = 1 Gyr × 0.2 dex.

2. For each mock field, we assign particles of given ages and [Fe/H] into the corresponding bins of the grid. We compute the total stellar mass associated to each bin, or single stellar population (SSP), as the sum of the particle's masses assigned to it.

3. For each age–[Fe/H] bin, we generate a synthetic SSP-CMD using IAC-STAR code (Aparicio & Gallart 2004), assuming a constant star formation rate and a uniform metallicity distribution. We adopted BaSTI stellar library (Pietrinferni et al. 2004) and a Kroupa (2002) initial mass function. We used the bolometric corrections by Bedin et al. (2005) to transform the theoretical tracks into the ACS/WFC photometric system.

4. Given the total mass associated with each bin, we need to calculate the number of stars that the corresponding SSP-CMD is contributing to the final mock-CMD. Note that the IAC-STAR code takes as input the number of stars rather than the mass of the simulated stellar system. Therefore, to realistically convert the BJ05 models into synthetic CMDs we need to calculate the corresponding number of stars using the stellar mass provided by the models. This was estimated using the LFs provided by Padova web interface CMD code (Marigo et al. 2008; Girardi et al. 2010). For a given SSP, the code provides an LF normalized to the initial stellar mass of the population. We multiply this LF by the total stellar mass associated with the SSP, which sets the number of stars needed.

5. Lastly, in order to make a fair comparison between the properties of observed stars and those predicted by the models, we simulate the observational effects (incompleteness and photometric errors) in the mock-CMDs. We follow the procedure described by Hidalgo et al. (2011 and references therein) for which each star in the mock-CMD is applied a magnitude and color correction from the AST results. The correction is the difference between the injected and recovered magnitudes of a randomly selected artificial star with similar injected magnitude, color, and position than the star in the mock-CMD.

We note that the simulated halos contain a non-negligible fraction of old (>10 Gyr) metal-poor stars ([Fe/H] < −2.2 dex). However, the stellar evolutionary models, and thus the isochrone database, do not contain stars with such low metallicities. We
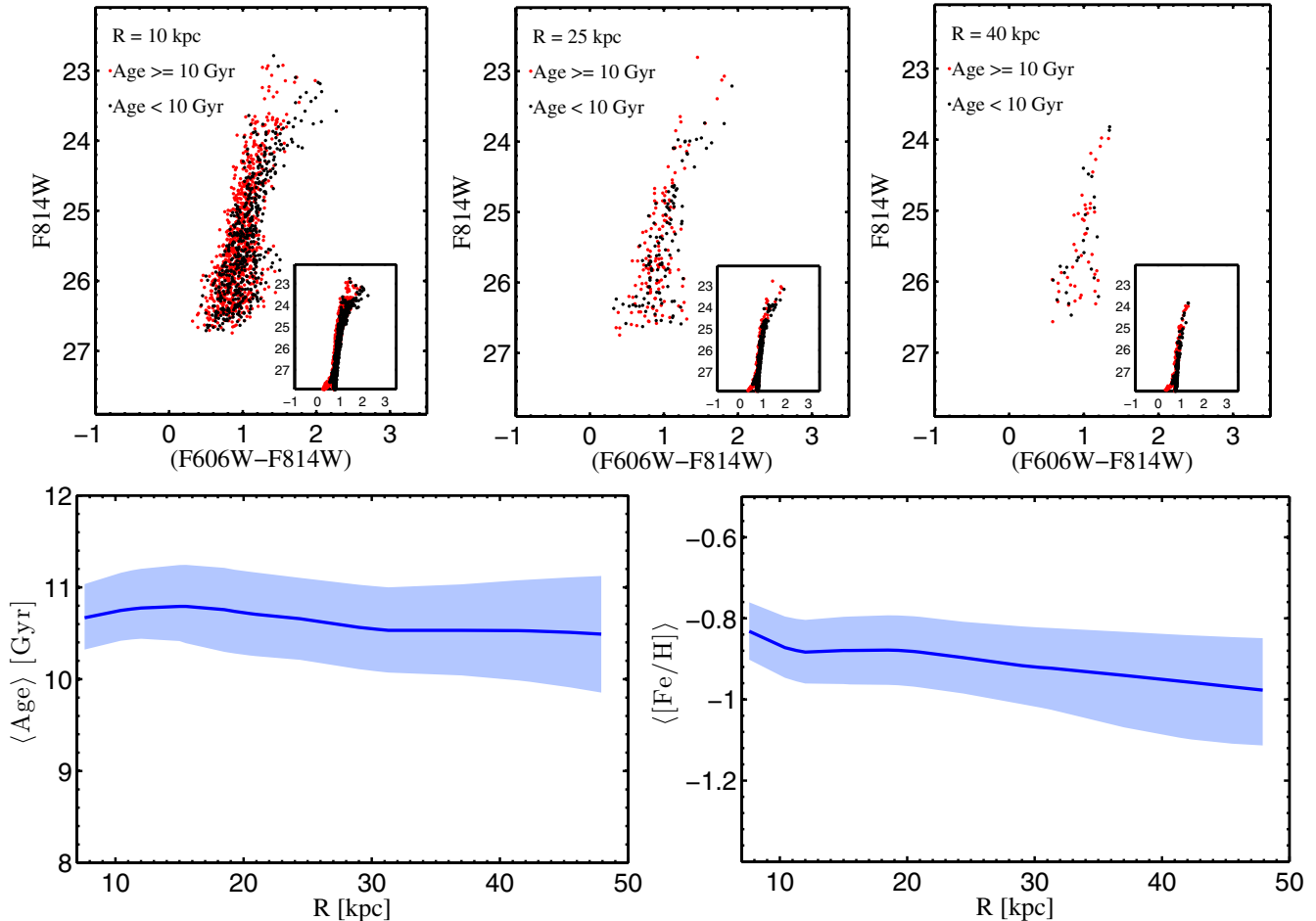
---

[11] http://www.astro.columbia.edu/~kvj/halos/

Figure 5. Top panel: three model CMDs of ACS-like fields generated from the stellar-halo model H1 by BJ05 at different galactocentric distances as indicated in each panel. Observational effects were simulated using the information provided by the ASTs, as described in the text. The insets show the model CMDs before simulating the observational effects. Red dots represent stars older than or equal to 10 Gyr, whereas black dots represent stars with ages between 7 and 10 Gyr. The first feature that we note from these CMDs is their narrow RGBs, despite the wide range of ages and metallicities predicted by the models (ages from ~6 to ~13.5 Gyr and metallicities $-4 <$ [Fe/H] < -0.4 for the particular halo model used here). Also, the younger stars preferentially exhibit redder colors than the older ones, which is expected due to their higher metallicities. Bottom panel: luminosity-weighted mean ages (left) and [Fe/H] (right) of the constructed CMDs. The solid lines indicate the mean ages and metallicities after averaging the results obtained for all 44 model fields, which accounts for the 11 halos placed at 4 different orthogonal directions. The shaded area indicates the 1σ model-to-model scatter from those means. The mean age remains roughly constant as a function of radius, whereas the mean metallicity becomes slightly more metal-poor at larger galactocentric distances, given the inside-out growth of the stellar halos assumed for the models.

(A color version of this figure is available in the online journal.)

have therefore assigned a metallicity of [Fe/H] $= -2.2$ dex to all the particles with metallicities lower than that value. Given the weak dependence of isochrone color on metallicity in this very low-metallicity regime (see Figure 2), this assumption should have little impact on the modeled CMD.

The top panel of Figure 5 shows three randomly chosen CMDs built using the first of the BJ05 halo realizations, H1, at distances of 10, 25, and 40 kpc from the galactic center. The insets show the corresponding model CMDs before the observational effects were simulated. Red dots indicate stars with ages older than or equal to 10 Gyr, whereas black dots indicate stars with ages between ~7 and 10 Gyr. Despite the significant mixture of populations predicted by the models, we note that the RGBs appear to be quite narrow (especially before simulating the observational effects). We find that this is always the case, regardless of the model that is used. This tightness results, at least partly, from the age–metallicity degeneracy. The younger stars, which should be bluer, are also more metal-rich and therefore have redder colors, which preserves the tightness of the RGB.

The bottom panel of Figure 5 plots the luminosity-weighted mean ages and metallicities of the model fields as a function of galactocentric distance. The solid lines indicate the average over all 11 halos, after placing the model fields at four different orthogonal directions in each halo, giving 44 values averaged in total. The shaded area represents the 1σ model-to-model scatter of those means.

The mean luminosity-weighted age is rather constant with radius, at ~10.6 Gyr, although there seems to be a mild decrease at larger radii. The average metallicity, however, shows a weak negative slope such that the mean metallicity is ~0.12 dex more metal-poor at $R \sim 50$ kpc. This gradient is a consequence of the modeled halo's merger history. The inner regions are assembled earlier from a few massive more metal-rich satellites, whereas satellites accreted at later times, which had preferentially more time to form stars and therefore contain younger stars, populate the halos at larger galactocentric distances (BJ05, Font et al. 2006a, 2008). BJ05 have shown that although the recent events represent a sub-dominant fraction of the total stellar halo luminosity (from ~5% to ~50%), they become the dominant contributor at radii of 30–60 kpc and beyond. Thus, the halos at

larger radii will have on average more metal-poor and somewhat younger populations.

6. COMPARING OBSERVATIONS WITH MODELS

We generate CFs and Gaussian distributions for the model CMDs exactly as we did for the observed ones, i.e., using the magnitude range and color index Q described in Section 4. We calculate the median colors in each of the model CMDs as well as the width of their CF distributions. We find that *the models do not predict a color gradient in the stellar halo.* Instead, the color distribution has a fairly constant median value of $(F606W - F814W) \sim 1.1$ at all galactocentric radii out to 50 kpc, as shown by the blue solid line in the top panel of Figure 4. This line shows the color profile of a typical stellar halo, constructed by averaging over all 11 halos at 4 orthogonal positions as explained in Section 5. Nevertheless, the models predict a small degree of scatter from model to model at a given radius, as shown by the shaded area which indicates the 1σ color deviation from the average value. This result is supported by our M81 observations for fields located at distances larger than 15 kpc, where we detect no color gradient and an approximately constant value with a small degree of variation from radius to radius.

We note that the observed median color of M81 appears to be slightly bluer than the averaged color predicted by the models. It is likely that this difference is due to oversimplifications in modeling the satellite galaxy formation and enrichment histories, coupled with differences in the assembly history of M81's halo with respect to the Milky-Way-like halo modeled by BJ05. In addition, it is possible that the metallicity floor adopted in the isochrones of [Fe/H] = −2.2 may also be partly responsible for this offset. In spite of the small mean color offset, however, it is important to emphasize that the models and observations do agree in the lack of a halo color gradient. The black dashed line in Figure 4 indicates the color profile, averaged over all modeled fields before simulating the observational effects. Comparing this line with the blue solid line shows that the average modeled colors become systematically redder once the observational effects are taken into account. This shift is likely due to the larger photometric errors of redder RGB stars compared to the bluer stars in the same $F814W$-magnitude range (the latter with brighter $F606W$ magnitudes).

The bottom panel of Figure 4 shows the comparison between the observed and modeled widths of the CFs as a function of galactocentric distance. The solid line and shaded areas indicate, as in the top panel, the average width and the 1σ model-to-model scatter for the model halos, respectively. The widths obtained from the modeled CFs are in good agreement with the observed values for fields located farther than 15 kpc from M81's center; interior to this, the observed CMDs are likely to have a substantial disk component, which is not included in the BJ05 halo models. The black dashed line indicates the average CF's width for the modeled fields before the observational effects were simulated, which is ∼0.2 mag. A color distribution width of ∼0.2 mag corresponds to a spread in metallicity of the order of ∼0.6 dex, as predicted by the halo models. The widths of the CFs are clearly larger after the observational effects are applied due to the photometric errors which broaden the RGBs. We note that at smaller radii the observational effects do not appear to significantly affect the CF widths. This is because the exposure time of fields, e.g., F9 and F2, which are at small radii, are much larger than the exposure time of most fields and therefore

their photometric uncertainty are smaller. The cyan circles show the CF widths of one of the halo models after simulating the observational effects. The cyan symbols lying on the black dashed line (which represents the modeled widths before the observational effects were simulated) are associated with the locations of the observed fields that have the largest number of exposures (fields F2, F9, and F12; see Table 1). Therefore, the broadening caused by observational errors on the widths of these particular CFs is almost negligible. In general, we find that the observed widths can be remarkably well reproduced by the models once the observational effects are taken into account. Given that the CF widths of the synthetic CMDs before the observational effects are simulated correspond to a metallicity spread, the good agreement between the observed and model widths, once the observational effects are taken into account, suggests that there may be a similar spread in metallicity (∼0.6 dex) in the observed M81 halo fields, even though the color distributions widen due to observational effects.

As discussed before, no color gradient is found in both the observed and modeled halos. However, within the hierarchical paradigm, the outer regions of halos ($R > 20$ kpc) are expected to have a noticeable spread in the ages and metallicities of their stellar populations (see, e.g., Font et al. 2008), mainly due to the presence of substructure in the form of cold stellar streams. Panoramic views of M31 (Ibata et al. 2007; McConnachie et al. 2009) have indicated that the presence of significant variations in the halo stellar populations can be associated with observed substructures (see, e.g., Brown et al. 2006; Richardson et al. 2008). Bearing in mind that the analysis in this work is based on pencil-beam *HST* observations, which sparsely sample M81's halo, we ask the following question. How likely is it that signatures of the substructure predicted by simulations, such as variations in the mean color of the stellar populations, are rendered difficult to observe due to the pencil-beam nature of these observations?

To address this question, we have built RGB maps of the entire halo, i.e., both smooth component and surviving satellites, at the distance of M81 considering the limiting magnitude of our *HST* observations, and oriented according to M81's inclination. Maps of the density of RGB stars for four different halo models, in a 100×100 kpc^2 XZ projection box, are shown in Figure 6. Each pixel in these images corresponds to an area of 0.5 kpc^2. From this figure, it is clear that the models predict a wealth of substructure in the distribution of RGB stars at M81's distance. Note that the amount of substructure strongly depends on the accretion history of each modeled halo. In Figure 7, we show the mean color distribution of the RGB stars plotted in Figure 6. The first four panels, from left to right, show the distribution of RGB stars on the sky found within different color ranges. These panels show that some substructures are more dominated by either redder or bluer stars than others. In the fifth panels we show maps of the mean colors of all RGB stars, after considering a bin size of 0.5 kpc^2, as in Figure 6. We note that there are no significant mean ($F606W - F814W$) color variations throughout each map; each halo seems to be dominated by one mean color, and departures from this mean are generally associated with surviving satellite galaxies orbiting the main halo. The situation becomes even worse when considering a bin size resembling that of the ACS/WFC field of view (FOV), as shown in the rightmost panels. Note that in this case the substructure has been virtually erased. There is a small degree of variation in the colors, with a maximal range from
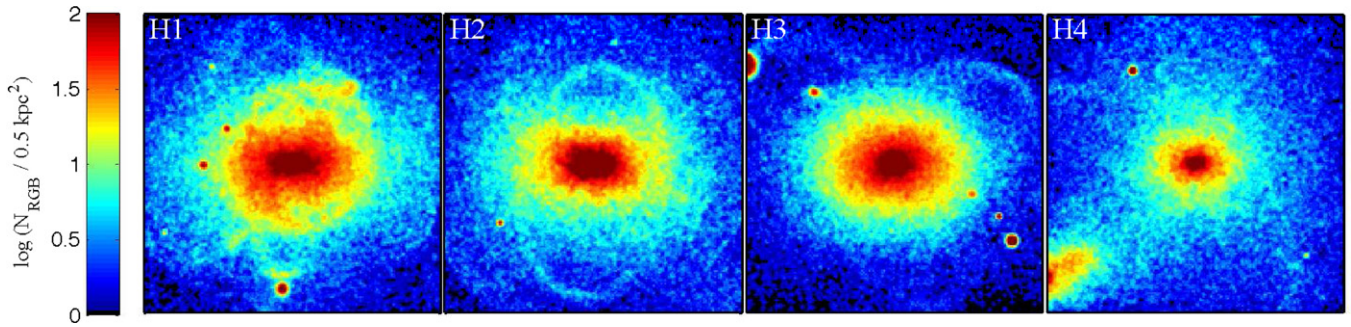
Figure 6. Density maps of modeled RGB stars, at the distance of M81, and rotated according to M81's inclination. Four different halo realizations were used, H1, H2, H3, and H4. The maps are shown in a 100×100 kpc^2 area, on the XZ projection. Each pixel in the images corresponds to 0.5 kpc^2. Clearly, substructure is expected from a distribution of M81-like RGB stars. Note that the amount of substructure varies from halo to halo, depending on accretion history.
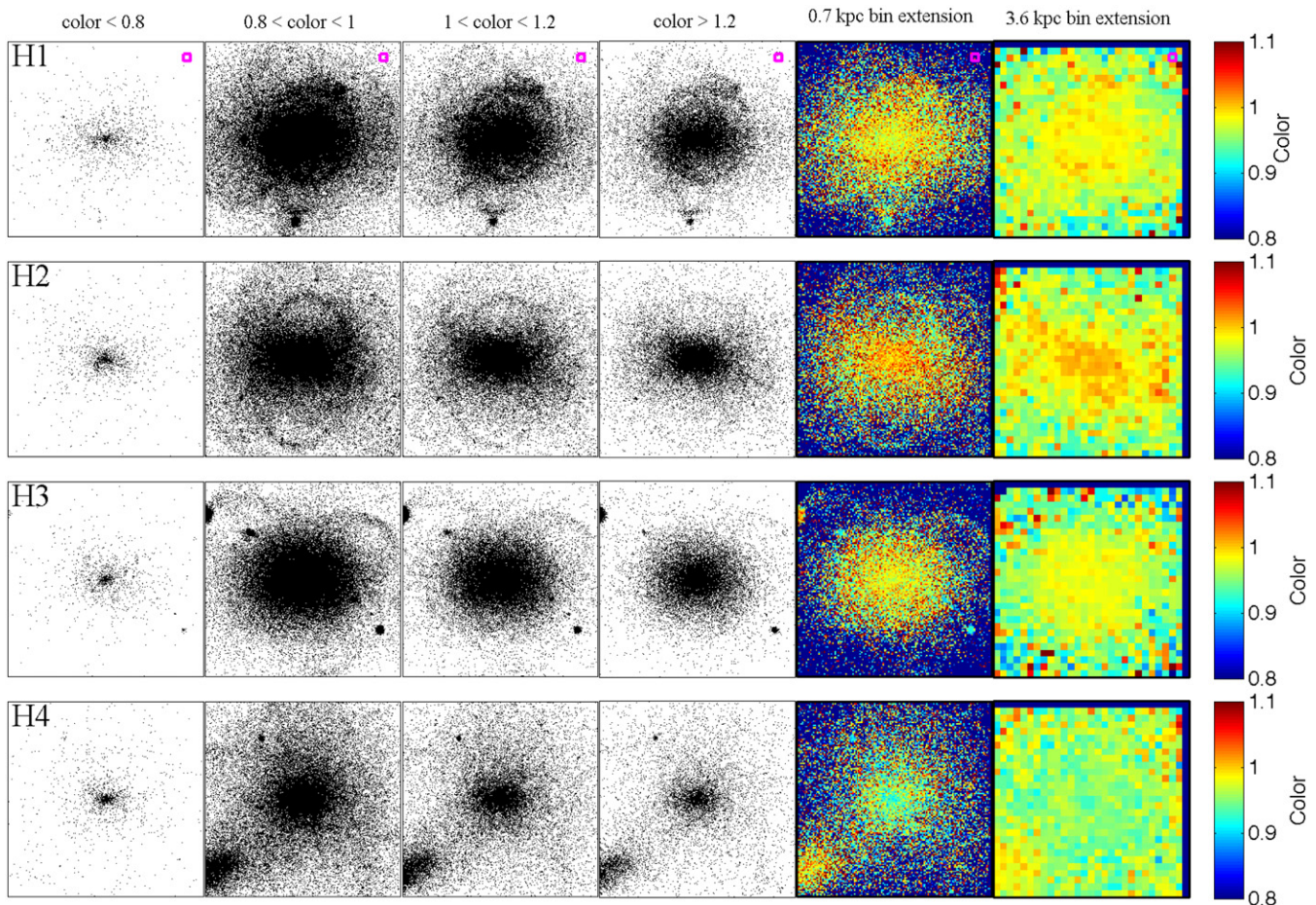

Figure 7. Color distribution of RGB stars at the distance of M81 for four halo realizations (from top to bottom). From left to right, the first four panels show the distribution of RGB stars within different color ranges. Some substructures are more dominated by either redder or bluer stars than others. The fifth panels show maps of the mean colors of all RGB stars with a bin size of 0.5 kpc^2. No significant variations in mean colors can be seen throughout each map. The rightmost panels show the mean color maps for a bin size of 3.6×3.6 kpc^2, resembling the size of the ACS/WFC FOV. Note that in this case the substructure has been virtually erased. The small degree of variation in the colors is challenging to detect with *HST* given the absolute calibration and shot-noise uncertainties. The magenta square shown in each of the top panels represents the extent of the ACS/WFC FOV at the distance of M81.

$\sim$0.95 to $\sim$1.1. Such subtle color differences are challenging to detect with *HST* given the absolute calibration and shot-noise uncertainties of $\sim$0.05 mag in ($F606W - F814W$) color. Note that the inner regions of these maps do not have median colors as red as the observations at $R < 15$. We recall that the models only simulate halo particles at all radii, whereas the M81 observations have significant contribution from the disk in the inner $R \sim 15$ kpc. The disk contribution, which is not included in the BJ05 models, is most likely responsible for the redder median colors of M81 observed at $R < 15$.

7. DISCUSSION

As shown in previous sections, we do not detect a color gradient in the stellar halo of M81. If we assume that the color profile of the RGB stars reflects the metallicity profile[12] of the stellar halo, our results suggest that there is no metallicity gradient in the halo of M81 within 15–50 kpc from the galactic center. We note that below [Fe/H] ~ -1, the expected color

---

[12] Even though there is a mixture of ages in the RGB, the colors of the RGB stars are more sensitive to metallicity than to ages.

variation due to metallicity changes is small for old populations ($\lesssim 0.2$ mag from [Fe/H] $= -1$ to ~ -2.5 dex), thus the data might be also consistent with a metallicity gradient to lower metallicity. Metallicities obtained using spectroscopic lines will generally better sample the more metal-poor component of an old system. However, we find a median color change of 0.03 ± 0.11 mag for the RGBs of the halo's fields within 15–50 kpc, which is consistent with no color as well as no metallicity gradient for old populations. The lack of a metallicity gradient is in agreement not only with the BJ05 models analyzed in this paper, but also with other theoretical studies based on accretion-only halos which found flat metallicity profiles (see, e.g., De Lucia & Helmi 2008; Cooper et al. 2010; Gómez et al. 2012).

On the other hand, Font et al. (2011) have analyzed $\sim 400\,L_*$ disk galaxies from cosmological hydrodynamical simulations, and found that the average stellar metallicity profile shows a prominent negative gradient over all radii, with the deepest decline (a ~ 0.4 dex metallicity difference) exhibited over the range of 20 kpc $< R <$ 40 kpc. They claim that the slope in the metallicity profile is induced by "in situ" star formation, which typically dominates at $R < 30$ kpc, whereas accretion of stars dominate at large radii. Our observations of M81 do no support such a strong gradient. In addition, even if one associates the redder stars that we observe in M81 (which clearly sample the properties of disk stars; see their CMDs in Figure 2), with an "in situ" formation, they appear not to extend further than ~ 15 kpc along the major axis, and not farther than ~ 10 kpc along the minor axis. From 15 to 50 kpc, i.e., the region studied in this work, Font et al. (2011) find a 0.7 dex metallicity difference in the spheroidal component of their simulated galaxies. Since they also find variations in the mean age with galactocentric distances, we explore whether their models predict a color gradient of RGB stars when both metallicity and age profiles are combined. Considering the median spherically averaged age and metallicity radial profiles provided by Font et al. (2011; see their Figures 5 and 10), we find that their results imply an intrinsic color difference of ~ 0.3 mag from 15 to 50 kpc with stellar halo RGB colors ($F606W - F814W$) becoming gradually bluer with increasing radius. This is not supported by our observations of M81 from 15 to 50 kpc.

We can compare our results with observations of halo stars in other large galaxies. For the Milky Way, there seems to be a discrepancy regarding whether or not a metallicity gradient exists. As discussed in Section 1, analysis of SDSS stars by Carollo et al. (2007, 2010) indicated a metallicity drop of ≈ 0.7–0.8 dex from the solar neighborhood out to ≈ 30–40 kpc. A different stellar halo sample from recent SDSS/SEGUE observations show a nearly flat Galactic halo metallicity distribution from ~ 20 kpc out to ~ 60 kpc with an average metallicity of [Fe/H] ~ -1.4 dex (Z. Ma et al., in preparation). Nevertheless, as mentioned in Section 1, these studies may have important biases introduced by, e.g., the magnitude or color limit considered, which affect the determination of a metallicity–distance relation (see, e.g., Schönrich et al. 2011). Thus, whether or not a gradient exists in the halo of the Milky Way is still unclear.

The metallicity of the stellar halo of M31 has also been extensively studied. Kalirai et al. (2006) and Koch et al. (2008) have detected a clear metallicity gradient with substantial scatter over a large range in radial distances, from ≈ 10 kpc with metallicity [Fe/H] ~ 0.5 dex to ≈ 160 kpc with [Fe/H] ~ -1.3 dex. However, as discussed in Section 1, photometric studies (see, e.g.,

Durrell et al. 2004; Irwin et al. 2005; Richardson et al. 2009) as well as spectroscopic studies (Chapman et al. 2006) found no detectable metallicity gradient from ≈ 10 to ≈ 60 kpc. Furthermore, the mean metallicity values vary from work to work (see Figure 6 of Richardson et al. 2009). It is unclear why the results are so diverse; differences probably arise from analysis of the data using different methods and techniques as well as from probing different various small regions of M31's halo, which is known to have a wealth of substructure and intrinsic metallicity variations. Overall, the inner ~ 15–50 kpc region of M31's halo seems to exhibit a nearly flat, high-metallicity profile ([Fe/H] ~ -0.8 dex), whereas outside ~ 60 kpc the metallicities are lower ([Fe/H] ~ -1.3 dex). It is interesting to note that both Irwin et al. (2005) and Guhathakurta et al. (2005) found two different structural components for the M31's spheroid. Stars at $R \lesssim 30$ kpc exhibit an $R^{1/4}$-power-law (or de Vaucouleurs) surface brightness profile whereas beyond that radius and out to ~ 160 kpc, the surface brightness profile flattens considerably and can be better fitted with an $R^{-2.3}$ power law. Kalirai et al. (2006) argue that the metal-rich and metal-poor components are respectively associated with the two different structural components.

Stellar halos of large early-type (E/S0) galaxies have also been studied. The halos of NGC 5128 and NGC 3377 show no metallicity gradients out to large galactocentric distances of ~ 40 kpc ($\sim 7\,R_e$) for NGC 5128 (Rejkuba et al. 2005) and ~ 18 kpc ($\sim 4\,R_e$) for NGC 3377 (Harris et al. 2007a), and both their mean metallicities are [Fe/H] ~ -0.6 dex. They contain virtually no stars more metal-poor than [Fe/H] ~ -1.5 dex. Harris et al. (2007b), on the other hand, studied the giant elliptical galaxy NGC 3379 and indicated the presence of a mild metallicity gradient, with low-metallicity stars ([Fe/H] $\lesssim -0.7$ dex) dominating in the outermost parts of their field, which reaches a projected distance of $\sim 12\,R_e$. In units of effective radius, this field is farther out than those analyzed for NGC 5128 and NGC 3377. Harris et al. (2007b) thus suggest that large early-type galaxies will have a diffuse, low-metallicity halo component detectable at radius larger than $\sim 10\,R_e$ from the galactic center.

The metallicity profiles observed for all the galaxies discussed, and the color profile detected in this work for M81, can be reproduced by simulated halos built entirely from accreted satellites. Cooper et al. (2010) find a diversity of metallicity gradient behaviors in their models, ranging from the lack of a detectable gradient to some systems with gradients or breaks or jumps in their metallicity profiles. Overall, there is little or no metallicity gradient when many satellites contribute comparably to the final halo, while metallicity profiles show steeper gradients or present sharp variations when only one or two massive satellites contribute significantly to the halo.

In short, the stellar halos of large galaxies display a great diversity of metallicity profiles, which reflects the stochasticity of halo mass assembly formation history.

8. SUMMARY AND CONCLUSIONS

We have analyzed 19 *HST* ACS fields in the outer disk and stellar halo of M81 from the GHOSTS survey, where the term M81's halo in this work denotes the faint, extended R^{-2} structural component detected by B09 and confirmed using the GHOSTS fields, which start to dominate the light at $R > 15.5$ kpc, i.e., ≈ 6 scale lengths (B09). These fields probe the stellar halo of M81 out to a projected radial distance as large as ~ 50 kpc from the galactic center. We have derived the

CF distributions of each of these fields. Fields closer than $R \sim 15$ kpc display redder median colors ($F606W - F814W \sim 1.3$) and typically wider CFs (width ~ 0.8 mag). A visual inspection of their CMDs, as well as their color profile shape as a function of major axis (see top panel of Figure 4), suggests that these fields are dominated by metal-rich disk stars. Fields located at $R > 15.5$ have nearly constant median color, consistent with being dominated by more metal-poor halo stars. *We do not detect any color gradient within the halo of M81 from 15 kpc out to 50 kpc.* There is, nevertheless, a small degree of scatter in the colors from field to field, but it is unclear whether this scatter is physical or due to instrumental uncertainties.

The halo of M81 is characterized by a color distribution of width ~ 0.4 mag and an approximately constant median ($F606W - F814W$) ~ 1 mag, fluctuating by less than ± 0.06 mag over a range of ~ 35 kpc. If we fit for a color gradient, we obtain a slope of -0.0009 ± 0.0031 mag/kpc, which places a limit of 0.031 ± 0.11 mag in the difference between the median color of RGB M81 halo stars at ~ 15 and at 50 kpc. This color gradient corresponds to a difference of 0.08 ± 0.35 dex in [Fe/H] over that radial range, if we assume a constant age of 10 Gyr.

We directly compared these results, assuming that what we observe is indeed the stellar halo of M81, with predictions by simulations of the formation of stellar halos, using the cosmologically motivated models provided by BJ05. From their predicted stellar populations which cover a wide range of ages and metallicities, we built synthetic CMDs of ACS-like fields, rotated by $60°$ to resemble M81's inclination, at different locations from 5 to 50 kpc. We simulated the observational effects to make a fair comparison with the observed data. The model CMDs display a narrow RGB, despite the mixture of populations predicted by the models.

After analyzing the synthetic stars in the same way as the data, we find that there is no color gradient in the models. The average color is ($F606W - F814W$) ~ 1.1 mag with a small degree of scatter within one halo model, as well as from model to model. This lack of a gradient is in very good agreement with the observations of M81 for fields at $R > 15$ kpc where the contamination from metal-rich disk stars becomes negligible. The widths of the CFs constructed from the models, which correspond to a spread in metallicity of the order of ~ 0.6 dex, are also in good agreement with the observations for these fields. This suggests that the observed M81 halo fields contain a similar spread in metallicity.

Since this work is based on pencil-beam observations, we investigated our sensitivity to detecting substructure with color distributions. For this purpose, we have built RGB star maps of different model halos at the distance of M81, considering the limiting magnitude imposed by *HST*. We find no significant mean color variations throughout these maps. Most of each halo appears to be dominated by one mean color and variations are generally related to stellar populations of surviving satellite galaxies orbiting the main halo. Much of this subtlety in color structure is driven by the age–metallicity anticorrelation of stars in the model halos, combined with the modest sensitivity of RGB ($F606W - F814W$) colors to variations in age and metallicity of the magnitude predicted by the models. This illustrates that measuring stellar population variations using RGB ($F606W - F814W$) colors in stellar halos will require stringent calibration and shot-noise uncertainties. We note, nevertheless, that the sensitivity of the RGB colors to variations in metallicity could be improved if a wider color baseline is used.

Finally, we note that our lack of detection of any significant color (and likely metallicity) gradient in M81's halo agrees well with many of the studies of M31's halo *within* the same galactocentric distances, i.e., from ~ 15 to ~ 50 kpc, as well as with the Z. Ma et al. (in preparation) study on the halo of our own Milky Way. The median metallicity that we find for M81's halo, [Fe/H] ~ -1.2 dex, however, is more metal-poor than that of the M31 halo ([Fe/H] ~ -0.8), but more metal-rich than that of the Milky Way stellar halo ([Fe/H] ~ -1.6), as measured between ~ 15 and ~ 50 kpc from the center of each galaxy. The observed differences are possibly due to the different assembly history that these galaxies may have had. Given that the Milky Way, M31, and M81 have similar luminosities (Karachentsev 2005; Mouhcine et al. 2005a), their different halo's metallicities seem to indicate a disagreement with the halo's metallicity–parent galaxy luminosity correlation reported by Mouhcine et al. (2005a). These results, on the other hand, are in agreement with the simulations by Renda et al. (2005), who predicted that at any given luminosity the metallicities of their simulated stellar halos (89 in total) span a range of ≈ 1 dex (see their Figure 1). They suggest that the diversity in halo metallicities arise from the differences in the galactic mass assembly histories.

The stochasticity of galaxy formation in a cosmological context results in a great diversity between the formation histories of the stellar halos. Large, nearby spiral galaxies appear to exhibit a wide variety of halo metallicities (see, e.g., Mouhcine et al. 2005b; Rejkuba et al. 2009). The GHOSTS data set provides important tests for current models of galaxy formation and evolution, since it enlarges the number of observed spiral galaxy's halos, required to obtain a more statistically significant sample for comparison with the different models. As shown in Figure 4, small color variations (due to age and metallicity variations) among different predicted halos are expected and different halo metallicities are also expected due to differences in the galactic mass assembly histories (see, e.g., Renda et al. 2005; Robertson et al. 2005; Cooper et al. 2010; Gómez et al. 2012). In a follow up paper, we will analyze the rest of the galaxies observed within the GHOSTS survey and we will quantify the scatter in the color profiles from observed halos as well as investigate whether there are correlations between the color or metallicity of the halo stars and the main halo properties, such as mass or morphological type.

Facility: HST (ACS)

REFERENCES

Aparicio, A., & Gallart, C. 2004, AJ, 128, 1465
Bailin, J., Bell, E. F., Chappell, S. N., Radburn-Smith, D. J., & de Jong, R. S. 2011, ApJ, 736, 24
Barker, M. K., Ferguson, A. M. N., Irwin, M., Arimoto, N., & Jablonka, P. 2009, AJ, 138, 1469 (B09)

Bedin, L. R., Cassisi, S., Castelli, F., et al. 2005, MNRAS, 357, 1038
Beers, T. C., Carollo, D., Ivezić, Ž., et al. 2012, ApJ, 746, 34
Bell, E. F., Xue, X. X., Rix, H.-W., Ruhland, C., & Hogg, D. W. 2010, AJ, 140, 1850
Bell, E. F., Zucker, D. B., Belokurov, V., et al. 2008, ApJ, 680, 295
Belokurov, V., Zucker, D. B., Evans, N. W., et al. 2006, ApJL, 642, L137
Bertin, E., & Arnouts, S. 1996, A&AS, 117, 393
Brown, T. M., Beaton, R., Chiba, M., et al. 2008, ApJL, 685, L121
Brown, T. M., Smith, E., Ferguson, H. C., et al. 2006, ApJ, 652, 323
Bullock, J. S., & Johnston, K. V. 2005, ApJ, 635, 931 (BJ05)
Bullock, J. S., Kravtsov, A. V., & Weinberg, D. H. 2001, ApJ, 548, 33
Carollo, D., Beers, T. C., Chiba, M., et al. 2010, ApJ, 712, 692
Carollo, D., Beers, T. C., Lee, Y. S., et al. 2007, Natur, 450, 1020
Chapman, S. C., Ibata, R., Lewis, G. F., et al. 2006, ApJ, 653, 255
Chiaberge, M., Lim, P. L., Kozhurina-Platais, V., Sirianni, M., & Mack, J. 2009, Updated CTE Photometric Correction for WFC and HRC, Technical Report
Cooper, A. P., Cole, S., Frenk, C. S., et al. 2010, MNRAS, 406, 744
Courteau, S., Widrow, L. M., McDonald, M., et al. 2011, ApJ, 739, 20
Dalcanton, J. J., Williams, B. F., Lang, D., et al. 2012, ApJS, 200, 18
Dalcanton, J. J., Williams, B. F., Seth, A. C., et al. 2009, ApJS, 183, 67
de Jong, J. T. A., Yanny, B., Rix, H.-W., et al. 2010, ApJ, 714, 663
De Lucia, G., & Helmi, A. 2008, MNRAS, 391, 14
de Mello, D. F., Smith, L. J., Sabbi, E., et al. 2008, AJ, 135, 548
Dolphin, A. E. 2000, PASP, 112, 1383
Durrell, P. R., Harris, W. E., & Pritchet, C. J. 2004, AJ, 128, 260
Durrell, P. R., Sarajedini, A., & Chandar, R. 2010, ApJ, 718, 1118
Ellis, S. C., & Bland-Hawthorn, J. 2007, MNRAS, 377, 815
Fardal, M. A., Babul, A., Geehan, J. J., & Guhathakurta, P. 2006, MNRAS, 366, 1012
Fardal, M. A., Guhathakurta, P., Babul, A., & McConnachie, A. W. 2007, MNRAS, 380, 15
Font, A. S., Johnston, K. V., Bullock, J. S., & Robertson, B. E. 2006a, ApJ, 638, 585
Font, A. S., Johnston, K. V., Ferguson, A. M. N., et al. 2008, ApJ, 673, 215
Font, A. S., Johnston, K. V., Guhathakurta, P., Majewski, S. R., & Rich, R. M. 2006b, AJ, 131, 1436
Font, A. S., McCarthy, I. G., Crain, R. A., et al. 2011, MNRAS, 416, 2802
Freedman, W. L., Madore, B. F., Gibson, B. K., et al. 2001, ApJ, 553, 47
Girardi, L., Williams, B. F., Gilbert, K. M., et al. 2010, ApJ, 724, 1030
Gómez, F. A., Coleman-Smith, C. E., O'shea, B. W., Tumlinson, J., & Wolpert, R. L. 2012, ApJ, 760, 112
Gómez, F. A., Helmi, A., Brown, A. G. A., & Li, Y.-S. 2010, MNRAS, 408, 935
Grillmair, C. J. 2009, ApJ, 693, 1118
Guhathakurta, P., Ostheimer, J. C., & Gilbert, K. M., et al. 2005, arXiv:0502366
Harris, W. E., Harris, G. L. H., Layden, A. C., & Stetson, P. B. 2007a, AJ, 134, 43
Harris, W. E., Harris, G. L. H., Layden, A. C., & Wehner, E. M. H. 2007b, ApJ, 666, 903
Helmi, A., & de Zeeuw, P. T. 2000, MNRAS, 319, 657
Helmi, A., & White, S. D. M. 1999, MNRAS, 307, 495
Helmi, A., White, S. D. M., de Zeeuw, P. T., & Zhao, H. 1999, Natur, 402, 53
Hidalgo, S. L., Aparicio, A., Skillman, E., et al. 2011, ApJ, 730, 14
Ibata, R., Martin, N. F., Irwin, M., et al. 2007, ApJ, 671, 1591
Ibata, R. A., Gilmore, G., & Irwin, M. J. 1995, MNRAS, 277, 781
Ibata, R. A., Irwin, M. J., Lewis, G. F., Ferguson, A. M. N., & Tanvir, N. 2003, MNRAS, 340, L21
Irwin, M. J., Ferguson, A. M. N., Ibata, R. A., Lewis, G. F., & Tanvir, N. R. 2005, ApJL, 628, L105
Ivezić, Ž., Sesar, B., Jurić, M., et al. 2008, ApJ, 684, 287
Johnston, K. V., Hernquist, L., & Bolte, M. 1996, ApJ, 465, 278
Jurić, M., Ivezić, Ž., Brooks, A., et al. 2008, ApJ, 673, 864
Kalirai, J. S., Gilbert, K. M., Guhathakurta, P., et al. 2006, ApJ, 648, 389
Karachentsev, I. D. 2005, AJ, 129, 178

Koch, A., Rich, R. M., Reitzel, D. B., et al. 2008, ApJ, 689, 958
Kroupa, P. 2002, Sci, 295, 82
Lacey, C., & Cole, S. 1993, MNRAS, 262, 627
Lin, D. N. C., & Faber, S. M. 1983, ApJL, 266, L21
Ma, Z., Morrison, H., Harding, P., et al. 2012, American Astronomical Society Meeting Abstracts, Vol. 219, 252.14
Majewski, S. R., Skrutskie, M. F., Weinberg, M. D., & Ostheimer, J. C. 2003, ApJ, 599, 1082
Marigo, P., Girardi, L., Bressan, A., et al. 2008, A&A, 482, 883
Martínez-Delgado, D., Gabany, R. J., Crawford, K., et al. 2010, AJ, 140, 962
Martínez-Delgado, D., Pohlen, M., Gabany, R. J., et al. 2009, ApJ, 692, 955
Mayer, L., Mastropietro, C., Wadsley, J., Stadel, J., & Moore, B. 2006, MNRAS, 369, 1021
McCommas, L. P., Yoachim, P., Williams, B. F., et al. 2009, AJ, 137, 4707
McConnachie, A. W., Irwin, M. J., Ibata, R. A., et al. 2009, Natur, 461, 66
Mouhcine, M., Ferguson, H. C., Rich, R. M., Brown, T. M., & Smith, T. E. 2005a, ApJ, 633, 821
Mouhcine, M., & Ibata, R. 2009, MNRAS, 399, 737
Mouhcine, M., Ibata, R., & Rejkuba, M. 2010, ApJL, 714, L12
Mouhcine, M., Rich, R. M., Ferguson, H. C., Brown, T. M., & Smith, T. E. 2005b, ApJ, 633, 828
Newberg, H. J., et al. 2009, BAAS, 41, 229
Newberg, H. J., & Yanny, B. 2005, in ASP Conf. Ser. 338, Astrometry in the Age of the Next Generation of Large Telescopes, ed. P. K. Seidelmann & A. K. B. Monet (San Francisco, CA: ASP), 210
Paturel, G., Petit, C., Prugniel, P., et al. 2003, A&A, 412, 45
Perryman, M. A. C., de Boer, K. S., Gilmore, G., et al. 2001, A&A, 369, 339
Pietrinferni, A., Cassisi, S., Salaris, M., & Castelli, F. 2004, ApJ, 612, 168
Radburn-Smith, D. J., de Jong, R. S., Seth, A. C., et al. 2011, ApJS, 195, 18 (RS11)
Rejkuba, M., Greggio, L., Harris, W. E., Harris, G. L. H., & Peng, E. W. 2005, ApJ, 631, 262
Rejkuba, M., Mouhcine, M., & Ibata, R. 2009, MNRAS, 396, 1231
Renda, A., Gibson, B. K., Mouhcine, M., et al. 2005, MNRAS, 363, L16
Richardson, J. C., Ferguson, A. M. N., Johnson, R. A., et al. 2008, AJ, 135, 1998
Richardson, J. C., Ferguson, A. M. N., Mackey, A. D., et al. 2009, MNRAS, 396, 1842
Robertson, B., Bullock, J. S., Font, A. S., Johnston, K. V., & Hernquist, L. 2005, ApJ, 632, 872
Robin, A. C., Reylé, C., Derrière, S., & Picaud, S. 2003, A&A, 409, 523
Sabbi, E., Gallagher, J. S., Smith, L. J., de Mello, D. F., & Mountain, M. 2008, ApJL, 676, L113
Sarajedini, A., Yang, S.-C., Monachesi, A., Lauer, T. R., & Trager, S. C. 2012, MNRAS, 425, 1459
Schlafly, E. F., & Finkbeiner, D. P. 2011, ApJ, 737, 103
Schlegel, D. J., Finkbeiner, D. P., & Davis, M. 1998, ApJ, 500, 525
Schönrich, R., Asplund, M., & Casagrande, L. 2011, MNRAS, 415, 3807
Tikhonov, N. A., Galazutdinova, O. A., & Drozdovsky, I. O. 2005, A&A, 431, 127
Tumlinson, J. 2010, ApJ, 708, 1398
Tyson, J. A. 2002, Proc. SPIE, 4836, 10
van der Hulst, J. M. 1979, A&A, 75, 97
Weisz, D. R., Skillman, E. D., Cannon, J. M., et al. 2008, ApJ, 689, 160
White, S. D. M., & Rees, M. J. 1978, MNRAS, 183, 341
Williams, B. F., Dalcanton, J. J., Seth, A. C., et al. 2009, AJ, 137, 419
Worthey, G. 1994, ApJS, 95, 107
Yanny, B., Newberg, H. J., Grebel, E. K., et al. 2003, ApJ, 588, 824
York, D. G., Adelman, J., Anderson, J. E., Jr., et al. 2000, AJ, 120, 1579
Yun, M. S. 1999, in IAU Symp. 186, Galaxy Interactions at Low and High Redshift, ed. J. E. Barnes & D. B. Sanders (Cambridge: Cambridge Univ. Press), 81
Yun, M. S., Ho, P. T. P., & Lo, K. Y. 1994, Natur, 372, 530